Progress in Additive Manufacturing
https://doi.org/10.1007/s40964-025-01012-9

FULL RESEARCH ARTICLE

Multi-physics simulation of a material extrusion-based additive manufacturing process: towards understanding stress formation in the printed strand

Mehul Lukhi[1] · Christoph Mittermeier[1] · Josef Kiendl[1]

Received: 31 July 2024 / Accepted: 4 February 2025

Abstract
The application of material extrusion methodologies in the fabrication of thermoplastic components frequently entails many notable challenges, such as shrinkage, warpage, and delamination. During the extrusion process, there is an uneven cooling gradient between the layers. As a result, this causes a component to be distorted. This deformation is observed as the corners of a component rise above the printing bed. However, printing a single-layer strand and then submerging it in hot water results in a noticeable distortion. This issue is explained, and it is investigated using simulations and experiments. The primary objective of this study is to conduct a numerical simulation of the extrusion process, with a specific emphasis on analyzing the stresses in the printed strand. The simulations are conducted utilizing the finite element approach, where the arbitrary Lagrangian–Eulerian method is employed to solve the free surface. Stress analysis entails solving the non-isothermal thermo-mechanical flow problem. The material extrusion process is simulated using generalized Newtonian and viscoelastic models. The present work aims to examine the spatial distribution of stresses inside the printed strand and its corresponding cross-sectional area. This study investigates the impact of several printing process parameters on stresses in the printed strand, including bed temperature, nozzle temperature, and printing speed. An experimental investigation was undertaken to examine the influence of printing speed on the degree of bending shown by the printed strand, with the aim of corroborating the results obtained through simulation. This study's findings provide valuable insights into the stresses experienced by the printed strand.

Keywords Material extrusion-based process · Viscoelastic flow · Arbitrary Lagrangian–Eulerian method · Stresses in the printed strand · Polylactic acid

1 Introduction

Additive manufacturing (AM), commonly known as 3D printing, refers to a variety of processes for depositing materials progressively to produce components. Researchers have produced various layer-by-layer deposition methods and materials. In 1988, Stratasys introduced material extrusion, subsequently labeled Fused Deposition Modeling (FDM) [1]. People are increasingly using material extrusion process to create small load-bearing structures, not just for quick prototyping. Therefore, it is critical to gain a deeper understanding of this process and the material properties that result from it.

Figure 1 depicts the material extrusion process, where the extruder injects filament into the liquefier. A liquefier's heating block turns solid material into liquid. A nozzle extrudes molten polymer onto the printing bed. This study examined material extrusion process and polymer deposition on the print bed using the Prusa i3 MK3 printer and polylactic acid (PLA) filament.

The viscoelastic characteristics of thermoplastic polymers enable them to undergo heat manipulation-induced stress storage and release. A thermoplastic polymer experiences

✉ Mehul Lukhi
mehul.lukhi@unibw.de

Christoph Mittermeier
christoph.mittermeier@unibw.de

Josef Kiendl
josef.kiendl@unibw.de

[1] Institute of Engineering Mechanics & Structural Analysis, University of the Bundeswehr Munich, Werner-Heisenberg-Weg 39, 85577 Neubiberg, Germany

Published online: 24 February 2025

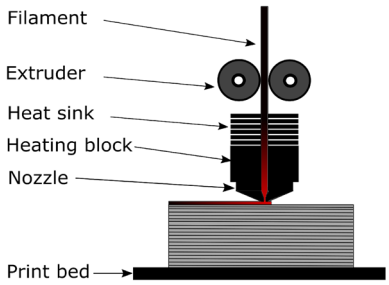

Fig. 1 Schematic diagram of the material extrusion process

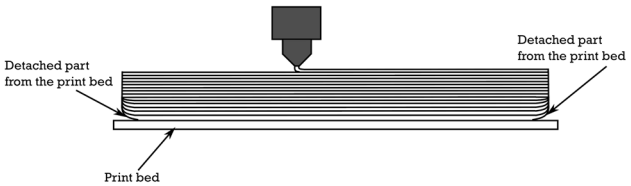

Fig. 2 Schematic diagram of a warping in the material extrusion process

the following during the material extrusion process: heating, shear, elongational behavior, and cooling. When a semi-crystalline polymer is cooled, the temperature decline causes shrinkage, which in turn causes internal stresses. Polymer viscoelasticity causes simultaneous relaxation. Stress evolution stops below the polymer's glass transition temperature. The numerical simulation of the extrusion process typically includes the polymer melting in the liquefier, the flow of molten polymer through the nozzle, the free extrusion (die swelling), and deposition on the print bed. Studying liquefier dynamics entails investigating temperature distributions and nozzle pressure drops. A lot of researchers, like Bellini [2], Turner et al. [3], Ji et al. [4], Atif Yardimci et al. [5], Ramanath et al. [6], Mostafa et al. [7], and Osswald et al. [8] have all used numerical simulations to study liquefiers. Since the Doi-Edwards (DE) reptation theory [9] was first introduced, there has been a lot more interest in studying polymeric flows, with a focus on how the viscoelastic properties of the liquid are taken into account. Researchers studied the shear and elongational properties of the polymer flow [10–17]. Tanner and Nasseri [15] compared the extended Pom-Pom, Giesekus, and Phan-Thien Tanner (PTT) models. The models have also been tested for their ability to explain complex polymer flow, shear, and elongation. Most researchers have described polymer flow in the liquefier as generalized Newtonian flow. This flow is characterized by shear-thinning and temperature-dependent viscosity variations. Thus far, viscoelastic constitutive material models are sparingly used to simulate polymer flow in material extrusion additive manufacturing processes. Phan et al. [18] assume viscoelastic behavior in molten polymer flow. A recent study by Serdeczny et al. [19] suggests that the viscoelastic model is more accurate than the Newtonian fluid model for analyzing liquefier dynamics in molten polymer flow.

To the authors' best knowledge, Bellini [2] completed the first completely resolved simulations of the material extrusion process. Numerous researchers have conducted detailed material extrusion process simulations [20–22]. To model material extrusion processes, different approaches have been used, such as the volume of fluid and finite element approaches (Bellini et al. [2], Watanabe [22], Serdeczny [20], Xia et al. [21], Comminal et al. [23], Liu et al. [24]). People commonly recognize the finite element technique-based ALE approach and the finite volume method as the most precise computational methodologies for predicting the form evolution of the printed strand. The techniques that rely on element activation do not accurately predict the shape of the printed strand. These methods are useful for estimating residual stress in printed components and examining how printing process patterns affect them. Except for Xia et al. [21] and Liu et al. [24], none of these approaches take into account the viscoelastic behavior of polymer melt during molten polymer deposition on the bed. While Xia et al. [25] examined residual stresses and shrinking volume during solidification, they did not consider print bed temperature. McIlroy et al. [26] assessed amorphous polymer melt deformation during extrusion and analyzed the associated stresses.

Temperature changes between printed layers might cause differential shrinkage and deformities. Insufficient adhesion can cause partial detachment from the print bed, as shown in Fig. 2. Numerous studies [27–30] attest to the fact that enormous amounts of research have been devoted to the phenomenon of warping using numerical, experimental, and analytical methods.

Van Manen et al. [31] studied the use of PLA, a thermoplastic polymer that can change shape in response to external stimuli. Changing the printing pattern and process parameters allowed the researchers to program the shape change of 3D-printed structures, known as 4D printing. Wu et al. [32] studied how printing speed and geometry affect the deformation of 4D printed shape memory polylactic acid (PLA). The researchers applied temperature stimuli to the printed geometry by immersing it in hot water. The stress differences between the upper and lower layers cause deformation.

The literature review indicates that researchers have employed viscoelastic material models to investigate polymeric flows. Few studies have used viscoelastic material models to simulate extrusion processes [18, 19, 21, 24, 26, 33]. The current studies lack comprehensive modeling of the extrusion process, including free surface modeling and the flow deposits on the heated bed. This work bridges the gap.

For this investigation, single strands were printed, let them cool down, and then removed it from the printing

surface. The current investigation did not detect the occurrence of warping. When removed from the printing surface, printed strands showed no evidence of distortion. The printed strands were immersed in hot water (368 K), above the glass transition temperature of PLA (341 K). They curled towards the print bed, as seen in Fig. 3b. Figure 3a depicts the printed filament's top view, while Fig. 3b shows the side view following its immersion in hot water. In this case, deformation is different from warping. The bending direction is towards the print bed. Due to the monolayer memory effect, the printed strand deforms. Crystallization occurs when PLA is gradually heated to a temperature around 363 K. In this instance, the quick heating process limits the crystallization of PLA. To confirm this, we repeated the process with the completely amorphous polymer polyethylene terephthalate glycol (PETG) and found the same behavior. The results demonstrate that crystallization does not cause bending. Moisture in hot water might distort the printed filament, but it is crucial to remember that absorption happens gradually, even at temperatures as high as 363 K. This information likely excludes moisture absorption and expansion as causes of the observed deformation behavior. These findings indicate that the deformation is caused by stresses which are stored in the material as a viscoelastic memory effect and released upon heating above glass transition temperature.

This study aims to develop an accurate extrusion process model and explanation for the one-layer memory effect (see Fig. 3). This study will determine the printed strand's upper, lower, and cross-sectional stress distributions. Polymer melt flow will be characterized by comparing the generalized Newtonian and viscoelastic material models' simulated extrusion processes. Multilayered part printing and deformation were not the focus of the study.

This article is organized as follows: In Sect. 2, the equations that control the flow with constitutive models are given. Section 3 describes the necessary material parameters for the constitutive models. Section 4 describes the printing process simulation model and associated constraints. This section focuses on the process of using simulations to determine stresses within the printed strand. The section also describes how different printing process parameters influence stresses within the printed strand. Section 5 demonstrates experimental verification of simulation results. The Section 6 summarizes the findings and suggests future study directions.

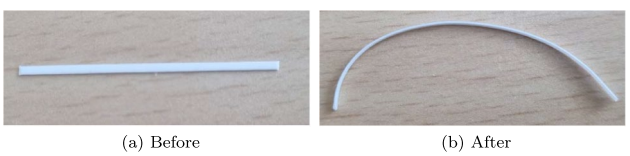

(a) Before (b) After

Fig. 3 Deformation of a single layer strand after it is immersed in the hot water

2 Mathematical description of polymer flow

The flow behavior of polymers in the extrusion process is characterized by the use of conservation equations and constitutive equations, as discussed by Bird et al. [34]. The three conservation equations, namely the continuity equation (mass conservation), balance of linear momentum, and energy conservation equations, are collectively referred to as the following Eqs. (1)–(3)

$$\frac{\partial \rho}{\partial t} + \nabla \cdot (\rho \boldsymbol{v}) = 0 \tag{1}$$

$$\rho\left(\frac{\partial \boldsymbol{v}}{\partial t} + \boldsymbol{v} \cdot \nabla \boldsymbol{v}\right) = -\nabla p + \nabla \cdot \boldsymbol{\tau} + \rho g \tag{2}$$

$$\rho C_{\mathrm{p}}\left(\frac{\partial T}{\partial t} + \boldsymbol{v} \cdot \nabla T\right) = \nabla \cdot (k \nabla T) + \boldsymbol{\tau} \cdot \nabla \boldsymbol{v}, \tag{3}$$

where the physical properties such as density (ρ), velocity ($\boldsymbol{v}$), pressure (p), extra-stress tensor ($\boldsymbol{\tau}$), gravitational constant (g), specific heat capacity (C_{p}), temperature (T), and thermal conductivity (k) are denoted by symbols. Equation (2) represents the principle of linear momentum conservation, wherein the momentum resulting from inertia is equilibrated by the forces exerted on the fluid flow. The aforementioned forces encompass pressure, viscous, elastic, and gravitational phenomena. The energy conservation in non-isothermal flow situations, where temperature evolution can be computed, is represented by Eq. (3). The heat transfer resulting from advection is equivalent to the combined heat transfer arising from conduction and convection, in addition to the heat generation caused by viscous dissipation. In simulations of material extrusion processes, the contribution of viscous dissipation is frequently neglected [20].

Polymers exhibit significant changes in density with temperature due to their high coefficients of thermal expansion. This equation captures this dependency, enabling accurate modeling of thermal effects on material behavior. The consideration of the change in density with temperature involves the utilization of the thermal expansion coefficient β, as indicated in Eq. (4)

$$\rho = \rho_0\big(1 - \beta(T - T_0)\big), \tag{4}$$

where ρ_0 is the density at reference temperature and T_0 is the reference temperature.

The Eqs. (1)–(3) in isolation do not provide a well-posed problem. To comprehensively handle this matter, it is necessary to incorporate supplementary equations that establish the relationship between flow deformation and the extra-stress tensor, as well as consider the influence of boundary and beginning conditions. This work examines the

constitutive equations governing generalized Newtonian and viscoelastic flow, which effectively address the aforementioned concern. The complete stress tensor, denoted as $\boldsymbol{\pi}$, can be decomposed into two distinct components: the hydrostatic component, which represents the pressure, and the deviatoric component, denoted as $\boldsymbol{\tau}$. This decomposition is discussed in Eq. (5)

$$\boldsymbol{\pi} = -p\boldsymbol{I} + \boldsymbol{\tau} \tag{5}$$

where $\mathbf{I}$ represents the identity tensor. In the context of a generalized Newtonian flow, the extra-stress tensor is contingent upon the instantaneous deformation and viscosity. Conversely, in viscoelastic flow, a memory effect is present, resulting in the extra-stress tensor being influenced by the immediate deformation, deformation history, and viscosity.

2.1 Generalized Newtonian flow

In the context of generalized Newtonian flow, the relationship between the extra-stress tensor, the rate of deformation tensor, and viscosity is expressed in Eq. (6) as discussed by Rudolph et al. [35] in their work on polymer dynamics.

$$\boldsymbol{\tau} = \eta(\dot{\gamma}, T)\boldsymbol{D} \tag{6}$$

$$\boldsymbol{D} = \nabla \boldsymbol{v} + \nabla \boldsymbol{v}^T \tag{7}$$

$$\dot{\gamma} = \sqrt{\frac{1}{2} I_2(\boldsymbol{D})}. \tag{8}$$

The symbols used in the equation are as follows: η represents the apparent viscosity, $\dot{\gamma}$ denotes the shear rate, $\boldsymbol{D}$ represents the rate of deformation tensor, and $I_2(\boldsymbol{D})$ represents the second invariant of the rate of deformation tensor. The viscosity of the majority of polymer fluids is contingent upon both the shear rate and temperature [35]. This research examines the relationship between viscosity and shear rate by employing the power law model. Additionally, the paper investigates the influence of temperature on viscosity.

$$\eta(\dot{\gamma}, T) = f(T)\eta(\dot{\gamma}) \tag{9}$$

$$\eta(\dot{\gamma}) = K\dot{\gamma}^{n-1}. \tag{10}$$

The power law, as stated in Eq. (10), characterizes the relationship between viscosity and shear rate. The flow behavior index (n) describes the fluid's behavior. In the case when n is a value smaller than one, the fluid exhibits shear-thinning characteristics, wherein the viscosity of the fluid drops as the shear rate increases. In the case where n exceeds 1, the fluid exhibits shear-thickening characteristics, wherein the fluid's viscosity increases as the shear rate increases. In the case where n is equal to 1, the fluid exhibits Newtonian characteristics. The flow consistency index (K) quantifies the viscosity of a flow under a shear rate of 1/s. The Arrhenius law and the Williams–Landel–Ferry (WLF) equation are widely recognized as the primary equations employed in the characterization of viscosity variation with temperature. The WLF equation is utilized to characterize the phenomenon of viscosity increase as a result of the cooling process, especially with regard to the glass transition. Both fully and partially amorphous or semi-crystalline thermoplastics, like polylactic acid (PLA), commonly exhibit this property. Equation 11 provides an improved iteration of the WLF equation, in which C_1 and C_2 represent the material constants, respectively [35]. The symbol T_a represents the temperature constant. The WLF equation is a mathematical expression that describes the relationship between a polymer's viscosity η at a specific temperature T and its viscosity at a reference temperature T_r.

$$\log(f(T)) = \frac{C_1(T_r - T_a)}{C_2 + T_r - T_a} - \frac{C_1(T - T_a)}{C_2 + T - T_a} \tag{11}$$

2.2 Viscoelastic flow

Polymeric fluids exhibit viscoelastic behavior [36]. Hence, the utilization of viscoelastic constitutive equations holds significant importance. In viscoelastic material modeling, the extra-stress tensor is decomposed to analyze viscoelastic, denoted as $\boldsymbol{\tau_1}$ and purely viscous, denoted as $\boldsymbol{\tau_2}$ contributions to deformation. This decomposition also simplifies computational implementation by splitting viscosity into two components. [34].

$$\boldsymbol{\tau} = \boldsymbol{\tau}_1 + \boldsymbol{\tau}_2 \tag{12}$$

The viscosity ratio (η_r) governs two aspects of viscosity. The calculation of the purely viscous term is performed using Eq. (16).

$$\eta = \eta_1 + \eta_2 \tag{13}$$

$$\eta_2 = \eta\eta_r \tag{14}$$

$$\eta_1 = (1 - \eta_r)\eta \tag{15}$$

$$\boldsymbol{\tau}_2 = \eta_2\boldsymbol{D} \tag{16}$$

The determination of a viscoelastic component, denoted as $\boldsymbol{\tau}_1$, is accomplished by utilizing a rheological model that is deemed appropriate for the specific application at hand. In the majority of practical scenarios, relying on a single constitutive equation is insufficient to adequately capture the stress relaxation characteristics shown by polymer flow. To accurately estimate the stress response of polymer flow, the viscoelastic component $\boldsymbol{\tau}_1$ is typically decomposed into

many modes [20]. Incorporating multiple modes allows viscoelastic models to capture the complex, time-dependent behavior of materials across various conditions. Experimental data, such as from dynamic mechanical analysis (DMA), often require multiple relaxation modes to accurately represent the observed behavior. When employing a multi-mode viscoelastic stress component, the first mode solely determines the purely viscous component of the extra-stress tensor. The viscosity is determined by the product of η and η_r.

$$\boldsymbol{\tau}_1 = \sum_{i=1}^{m} \boldsymbol{\tau}_1^i \tag{17}$$

The viscoelastic component $\boldsymbol{\tau}_1$ is determined in this study utilizing the exponential form of the Phan-Thien and Tanner (PTT) model. The PTT viscoelastic model is a differential model that is rooted in network theory, originally described in [37]. This model incorporates shear viscosity and elongation characteristics, which are helpful in characterizing the shear and elongation properties of polymer flow during the extrusion process.

$$exp\left(\frac{\epsilon_i \lambda_i}{\eta_1^i} tr(\boldsymbol{\tau}_1^i)\right)\boldsymbol{\tau}_1^i + \lambda_i\left[\left(1-\frac{\xi_i}{2}\right)\overset{\Delta}{\boldsymbol{\tau}}_1^i + \frac{\xi_i}{2}\overset{\nabla}{\boldsymbol{\tau}}_1^i\right] = \eta_1^i \boldsymbol{D} \tag{18}$$

The symbols $\overset{\Delta}{\boldsymbol{\tau}}_1^i$ and $\overset{\nabla}{\boldsymbol{\tau}}_1^i$ represent the lower- and upper-convected time derivatives, respectively. The constitutive model is described by the upper- and lower-convected time derivatives, which ensure objectivity and indifference to the material frame. They are mentioned in Eqs. (19) and (20). The variable ξ characterizes the shear response of polymer network junctions, namely the degree of slip that occurs. On the other hand, the variable ϵ represents the polymer's elongation, which is a measure of its extensibility. The symbol λ represents relaxation time. The effective slip refers to the relative motion between the polymer chains and the viscous medium. The temperature has a direct influence on the viscoelastic properties, such as relaxation time and viscosity. The impact of temperature on viscoelastic parameters is analyzed using the WLF equation stated in Eq. (11).

$$\overset{\Delta}{\boldsymbol{\tau}}_1^i = \frac{D\boldsymbol{\tau}_1}{Dt} + \boldsymbol{\tau}_1^i \cdot \nabla v^T + \nabla v \cdot \boldsymbol{\tau}_1^i \tag{19}$$

$$\overset{\nabla}{\boldsymbol{\tau}}_1^i = \frac{D\boldsymbol{\tau}_1}{Dt} - \boldsymbol{\tau}_1^i \cdot \nabla v - \nabla v^T \cdot \boldsymbol{\tau}_1^i \tag{20}$$

3 Material parameters

The study employs PLA in the material extrusion process. To conduct a numerical investigation of this process, it is critical to accurately describe PLA's rheological properties. This entails specifying the parameters for constitutive models such as the power law, PTT model, and WLF equation. The rheological data for PLA was acquired from the literature [38] and extracted from the curves. Subsequently, the data was fitted to Eqs. (10), (11), and (18) using the Ansys Polymat tool. The acquired parameters are displayed in Tables 1 and 2.

4 Printing process simulation

4.1 Simulation setup

The schematic diagram shown in Fig. 4 depicts the process of molten polymer extrusion through the nozzle and its subsequent deposition on the print bed. The diagram depicts a cross-sectional perspective of the nozzle and print bed. This study utilizes the commercially available Ansys Polyflow program for performing the simulations. The simulation model encompasses the internal section of the nozzle component, which consists of molten polymer. Additionally, it encompasses the section of the nozzle depicted as a black rectangle in Fig. 4. This section compresses the printed strand. The print bed and black rectangle depicted in Fig. 4 are represented as bodies, with temperature being the degree of freedom. These bodies remain rigid and do not undergo any deformation. The model represents only one side of the nozzle and print bed due to symmetry along the XY plane. The flow of the molten polymer is characterized by both generalized Newtonian flow and viscoelastic flow, which are being compared. The goal of this study is to understand the stresses present in the printed strand and determine the best material model for elucidating them.

The molten polymer region is divided into discrete elements using a fixed mesh, as depicted in Fig. 4. On the other hand, the region with a free surface, as indicated in

Table 1 Power law and WLF law parameters

Parameter	Symbol	Value
Consistency index	K	3594.56 Pas^n
Power law index	n	0.7766
WLF constant 1	C_1	10.25
WLF constant 2	C_2	625 K
Reference temperature	T_r	448 K
Temperature constant	T_a	298 K

Table 2 4 Modes PTT model parameters

Parameter	Symbol	Mode 1	Mode 2	Mode 3	Mode 4
Viscosity	η	1408.52 Pa s	519.71 Pa s	52.84 Pa s	8.790 Pa s
Viscosity ratio	η_r	0.12	0	0	0
Relaxation time	λ	0.01 s	0.1 s	1 s	10 s
Shear viscosity behaviour parameter	ξ	0.3682	0.3187	0.1933	0.0120
Elongational behavior parameter	ϵ	0.0112	0.0092	0.09473	0.0106

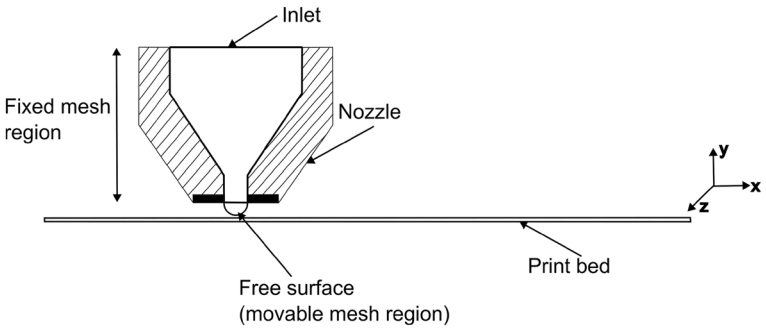

Fig. 4 Schematic diagram of the extrusion through the nozzle and deposition on the print bed

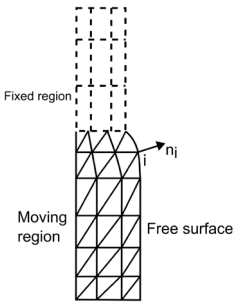

Fig. 5 Normal direction at the node

Fig. 4, is discretized using a moving mesh. The arbitrary Lagrangian–Eulerian (ALE) formulation on the surface handles the moving mesh. This formulation employs a Lagrangian technique for handling nodes in the normal direction and an Eulerian approach for nodes in the other direction. The Fig. 5 illustrates the typical orientation of the node on the free surface. The mesh region in motion undergoes remeshing at each time step. We use tetrahedral elements to mesh the inside of the nozzle and the moving mesh region. The print bed and external portion of the nozzle, indicated as a black rectangle in Fig. 4, are meshed using brick elements. The tetrahedral elements have velocities ($\boldsymbol{v}$), pressure (p), and temperature (T) as degrees of freedom. Figure 6 displays the simulation model's mesh.

Upon exiting the nozzle, the liquefied polymer makes contact with the print bed and undergoes compression. The black rectangular component depicted in Fig. 4 also makes contact with the polymer that has been deposited and causes it to become flattened. The simulation defines the potential contact areas between the nozzle and the extrudate, as well as between the print bed and the extrudate. A penalty mechanism enforces the interaction. Ansys Polyflow selects the parameters for the penalty approach. The implicit Euler technique solves the system of equations in a fully coupled manner. In the simulation, the print bed

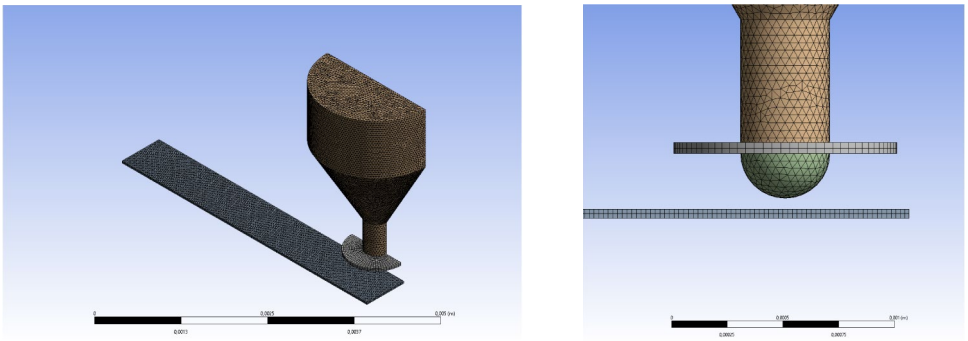

(a) Mesh of the simulation model

(b) Detail of the mesh near nozzle outlet and print bed

Fig. 6 Meshed printing process model

is set to a specific print velocity while the nozzle remains stationary, as described in the literature [2, 20].

The flow boundary conditions are given as follows:

- At the domain inlet, a constant volumetric flow rate with a fully developed flow profile is imposed. The volumetric flow rate is calculated using an Eq. (21)

$$\dot{Q} = \frac{\pi}{4} D_{\mathrm{f}}^2 \dot{E} \tag{21}$$

  where $\dot{Q}$ is a volumetric flow rate, D_{f} is the filament diameter and $\dot{E}$ is the feed rate.
- Along the nozzle wall, the no-slip velocity boundary condition ($\boldsymbol{v}_n = \boldsymbol{v}_s = 0$) is imposed.
- On the extrudate, a free surface boundary condition (zero surface tractions and no flow normal to the surface $\left(\frac{\partial \boldsymbol{x}}{t} - \boldsymbol{v}\right) \cdot \boldsymbol{n} = 0$) is imposed.
- There is a contact between the extrudate and the print bed.

The thermal boundary conditions are given as follows:

- At the domain inlet, the temperature is imposed (478 K) unless specified other value.
- Along the nozzle wall, the temperature is imposed (478 K) unless specified other value.
- On the extrudate, the convection heat transfer boundary condition is imposed (heat transfer from printed strand to the environment).
- The temperature is imposed on the print bed (293 K) unless specified other value.
- After establishing the contact, $\alpha * (T - T_{\mathrm{bed}})$ provides the heat flux between the extrudate and the print bed.

The simulations for the printing process utilize generalized Newtonian and viscoelastic material models. These models consider a variety of printing process factors, including flow rate, printing speed, nozzle temperature, bed temperature, and convection coefficient. The parameters of the printing process are as follows: The flow rate ($\dot{Q}$) is 25.13 mm^3/s, the printing speed (V_p) is 50 mm/s, the layer height (z) is 0.25 mm, the convection coefficient (h) is 30 $\mathrm{W}/(\mathrm{m}^2\mathrm{K})$, and the ambient temperature (T_{ambient}) is 303 K. According to the Ansys polyflow manual, the value of $\alpha = k/z$ is 1000 $\mathrm{W}/(\mathrm{m}^2\mathrm{K})$. Thermal conductivity of PLA is 0.25 $\mathrm{W}/(\mathrm{mK})$. The simulation results for both material models, along with their respective temperature distributions, are displayed in Fig. 7.

4.2 Comparison of Newtonian and viscoelastic material models

The temperature profiles along the printed strand are shown in Fig. 7, which uses the printing parameters already mentioned to compare the generalized Newtonian and viscoelastic models. Upon extrusion, the flow quickly dissipates heat and approaches ambient temperature, as seen in Fig. 7. Friction between the molten polymer and the nozzle wall impedes the flow, causing the polymer chains to elongate. The primary cause of stretching occurs when the polymer flow diameter decreases from 1.75 mm filament diameter to 0.4 mm nozzle diameter during the material extrusion process. It is visible in Fig. 8. When there is sufficient space between the nozzle and print bed, the polymer flow makes a 90° bend. The streamlines show that the outer section of the nozzle compresses the polymer flow, resulting in a flat top surface of the printed strand. The flow rate, printing speed, nozzle-to-print bed distance, and nozzle diameter all have a significant impact on strand morphology. Additional printing

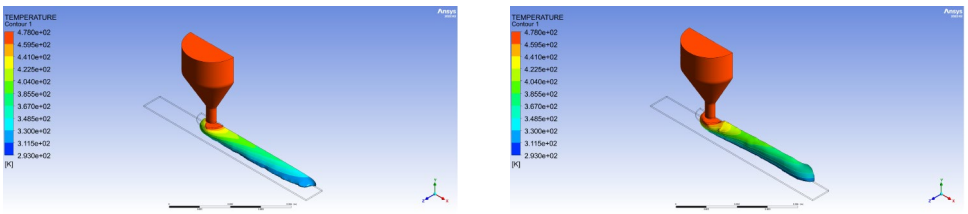

(a) Generalized Newtonian flow simulation (b) Viscoelastic flow simulation

Fig. 7 Printing process simulations with two different material models with temperature distribution

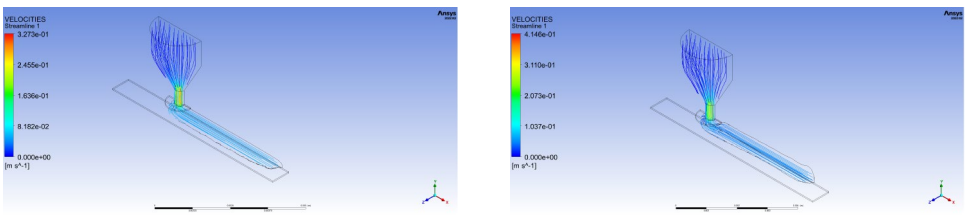

(a) Generalized Newtonian flow simulation (b) Viscoelastic flow simulation

Fig. 8 Streamlines in the printing process model simulation

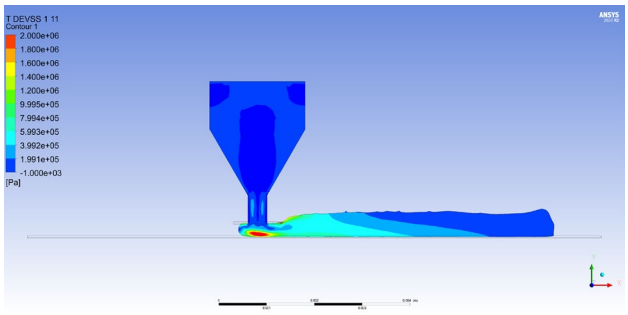

Fig. 9 Residual stress distribution across the cross-section

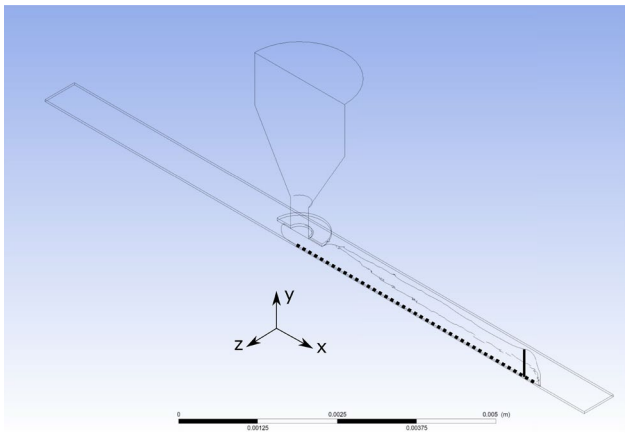

Fig. 10 The path at which different variables are extracted

factors, such as nozzle temperature, bed temperature, and cooling rate, have minimal impact. Figure 9 shows the nozzle and printed strand cross-section along the symmetry plane.

During the post-processing of the material extrusion process simulation, numerous variables such as pressure, shear rate, and stress are acquired from the path generated on the print bed, as represented in Fig. 10 with a horizontal dashed line. Figure 11 shows a significant decrease in pressure and shear rate. The release of stresses during the printing process occurs when the polymer flow, given by the generalized Newtonian model, is no longer subjected to deformation after exiting the nozzle.

The stress tensor's diagonal components primarily signify the pressure and have a greater influence in comparison to the shear components of the stress tensor. This phenomenon is observable in Fig. 13. The distribution of stress across the length of the cross-section is depicted in Fig. 14a. The stress component τ_{11} across the height of the cross-section is depicted in Fig. 14b. The τ_{11} values are obtained from the line located at a specific distance from the nozzle, as depicted in Fig. 10 as a vertical line. The simulations are conducted using the symmetric model, whereas the complete model has been created solely for the purpose of visualization. Significant stress at the printing bed and minimal stress at the top surface mark the stress distribution across the cross-section's height. This behavior is due to the discrepancy in deformation between the strand's upper and lower surfaces. At higher temperatures, these stresses may dissipate, but they freeze when the material cools down. Heat can cause stresses to release, resulting in a change in the shape and/or size of the printed item. This phenomenon is commonly referred to as the 4D printing effect.

The generalized Newtonian and viscoelastic material models were used to simulate the extrusion process. The results showed that the flow of polymer goes through about 90° deformation, stretching, and squeezing. Polymer chains deform, causing stress in the polymer flow. There are no characteristics in the generalized Newtonian material model that can account for this deformation. It is unable to simulate the stress present in the polymer flow. Upon examining the outcomes of the generalized Newtonian and viscoelastic

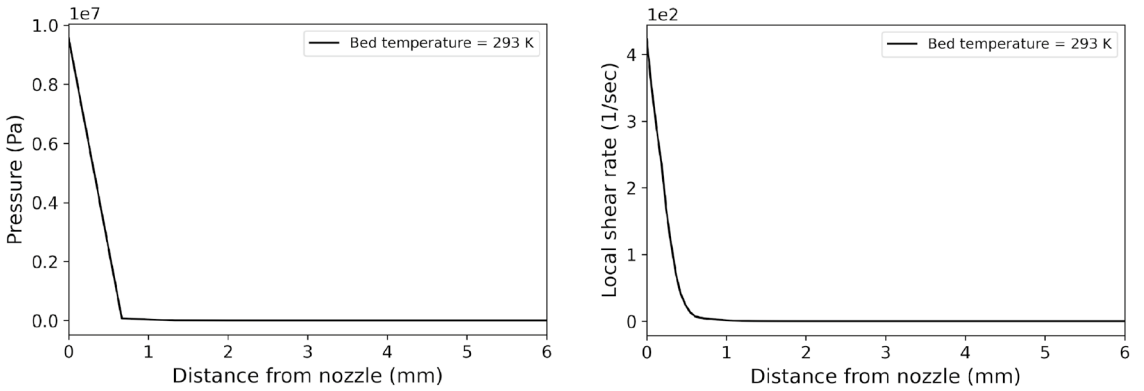

(a) Pressure vs. distance from the nozzle center

(b) Shear rate vs. distance from the nozzle center

Fig. 11 Pressure and shear rate distribution on the printed strand for the generalised Newtonian flow simulation

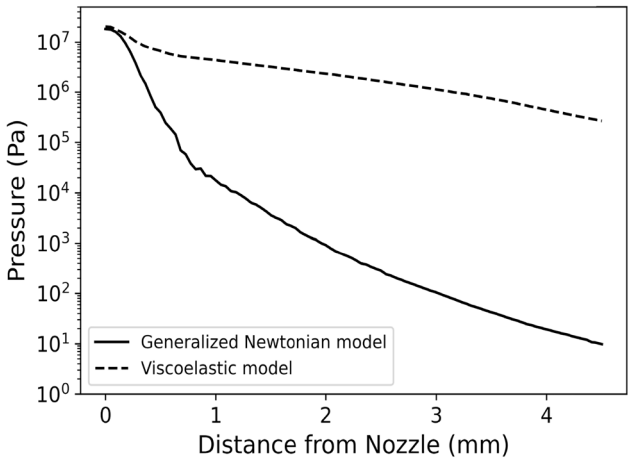

Fig. 12 Pressure distributions along the printed strand for the generalised Newtonian and viscoelastic flow simulations

flow simulations depicted in Fig. 12, it becomes apparent that there is a noticeable disparity in the pressure evolution between the generalized Newtonian and viscoelastic models. The solid line depicts the pressure distributions of the generalized Newtonian flow simulation, whereas the dotted line shows the pressure distributions of the viscoelastic flow simulation. The solid line exhibits a steep decline as it falls over the cliff, whereas the dashed line shows a steady reduction. This suggests that the viscoelastic model effectively maintains both pressure and viscoelastic stresses, as depicted in Fig. 13. The PTT model has many modes with varying relaxation times and viscosities to maintain the viscoelastic stresses. If material extrusion process modeling aims to examine the morphology of the printed strand, both generalized Newtonian and viscoelastic models are appropriate. However, applying generalized Newtonian models is insufficient for accurately predicting the stress distribution within a printed strand. To investigate stress within a printed strand, it is imperative to employ an appropriate viscoelastic material model.

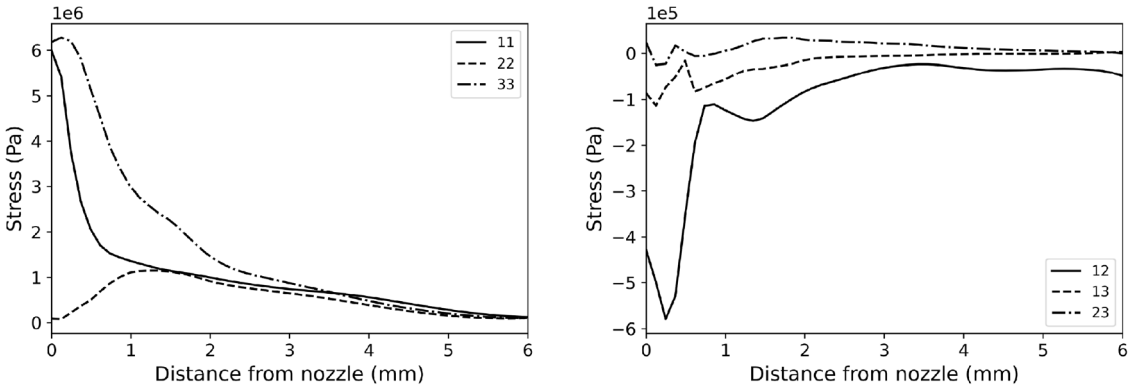

(a) Diagonal components of viscoelastic stress tensor vs. distance from the nozzle

(b) Off-diagonal components of viscoelastic stress tensor vs. distance from the nozzle

Fig. 13 Viscoelastic stress tensor components for the viscoelastic flow simulation

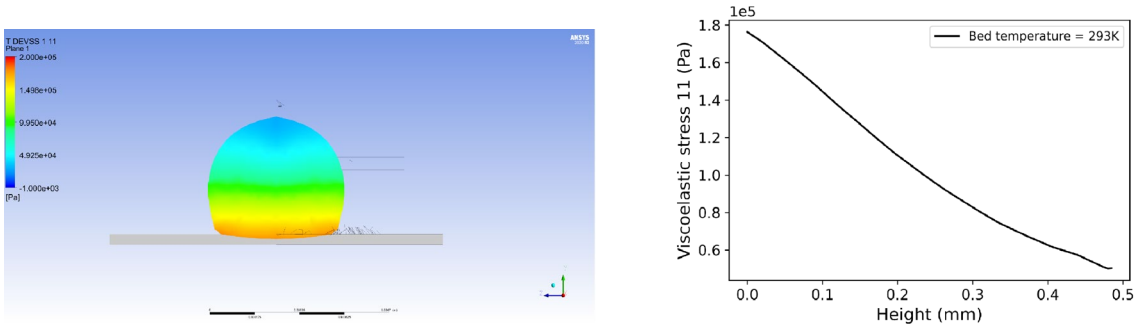

(a) Cross-sectional view of printed strand with viscoelastic stress tensor component 11 distribution

(b) Von Mises viscoelastic stress across the height of printed strand

Fig. 14 Stress component 11 distribution across the height of printed strand

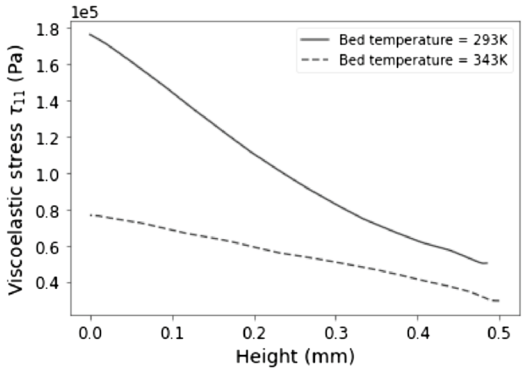

(a) Residual stress distribution for two different bed temperatures

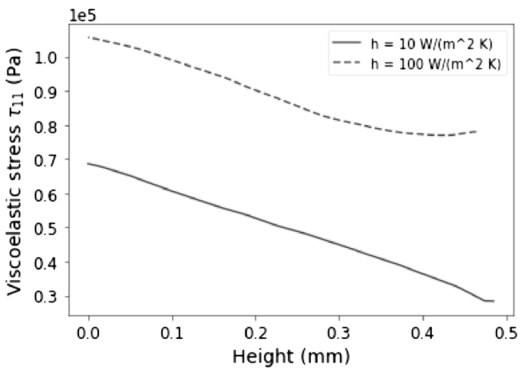

(b) Residual stress distribution for two different convection coefficients

Fig. 15 Viscoelastic stress tensor component τ_{11} distributions along the height of printed strand for two different bed temperatures simulations and two different convection coefficients simulations

This simulation model was utilized to depict the development of the free surface and stress distribution within the strand. Previous studies have not documented this phenomenon. The PTT model enables an accurate depiction of stress distribution in the printed strand by incorporating shear and elongation characteristics, viscosity, and relaxation time parameters. The simulation shows elevated stress levels on the print bed and reduced stress levels on the top surface. The uneven distribution of stress along the height of the printed strand causes it to bend towards the print bed when heated above the glass transition temperature of PLA. This phenomenon exhibits dissimilarities in the warping of components in 3D printing.

The parametric study examines the influence of several printing process factors, including bed temperature, convection coefficient, printing speed, and nozzle temperature, on residual stresses in the material extrusion process. The subsequent simulations are conducted via a viscoelastic material model. The printing process parameters for the following simulations are as follows: nozzle temperature of 478 K, bed temperature of 313 K, printing speed of 50 mm/s, volumetric flow rate of 16 mm^3/s, and convection coefficient of 30 $W/(m^2K)$, unless otherwise stated.

4.3 Parametric studies

The following printing process parameters are widely recognized for their significant influence on the efficiency of the printing process, as well as the mechanical properties and appearance of 3D-printed parts:

- Nozzle Temperature
- Bed Temperature
- Layer Height
- Print Speed
- Cooling Rate (convection coeff.)
- Infill Density and Pattern

Among these, nozzle temperature, bed temperature, print speed, and cooling rate were identified as the most critical factors influencing stress formation in printed strands. This study focuses on single-strand printing; hence, these parameters were prioritized for the parametric analysis. To ensure consistent cross-sectional geometry and isolate the effects of the selected parameters, layer height was kept constant.

4.4 Bed temperature

Computational simulations were performed to examine the influence of bed temperature on stresses in the printed strand. The simulations were conducted using the parameters indicated above, employing two distinct bed temperatures: 293 K and 343 K. The black vertical line in Fig. 10 is used to collect stresses at a distance of 5 mm from the center of the nozzle. The plot in Fig. 15a represents the viscoelastic stress tensor component τ_{11} as a function of the printed strand's height. As previously stated, the lower section of the strand undergoes more deformation than the upper section. The bottom of the strand (at the print bed) is more stressed than the top of the strand. The distribution of stress along the height of the print strand is depicted in Fig. 15. The curve depicted in Fig. 15a demonstrates a negative correlation between elevated bed temperature and reduced stresses. The reduced stresses in the printed strand can be attributed to the longer relaxation time available at higher bed temperatures, which facilitates more stress release. Increasing the print bed temperature reduces stress within the printed strand, leading to significant improvements in print quality. These include enhanced bed adhesion, reduced warping, better dimensional

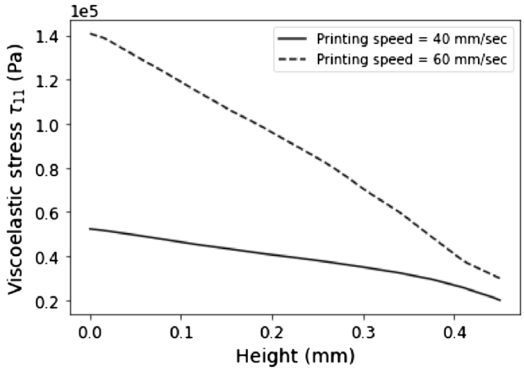

(a) Residual stress distribution for two different printing speeds

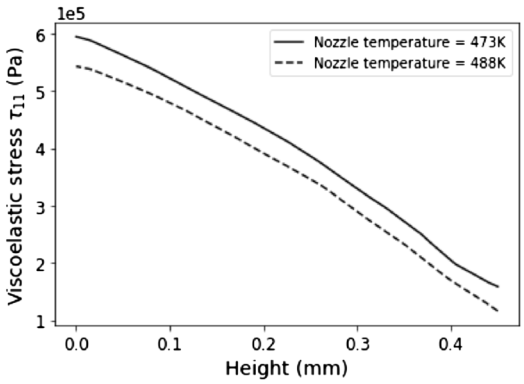

(b) Residual stress distribution for two different nozzle temperatures

Fig. 16 Viscoelastic stress tensor component τ_{11} distributions along the height of printed strand for two different printing speeds simulations and two different nozzle temperatures simulations

accuracy, and improved mechanical properties. However, optimizing the bed temperature for specific materials and print conditions is critical to maximizing these benefits while avoiding potential drawbacks. Excessively high print bed temperatures in 3D printing can cause material overheating, warping, dimensional inaccuracies, and adhesion issues, compromising part quality and print reliability.

4.5 Convection coefficient

Computational simulations were performed to examine the influence of the convection coefficient on stresses in the printed strand. The simulations were conducted using the aforementioned parameters and heat transfer coefficients of 10 and 100 W/(m^{2}K). The heat convection coefficient for natural convection between air and polymer extrudate often falls within the range of 2.5–25 W/(m^{2}K), whereas for forced convection between air and polymer extrudate, it typically falls within the range of 10–500 W/(m^{2}K). For this study, the values of 10 and 100 W/(m^{2}K) are selected. For stress extraction, the black vertical line in Fig. 10 is used. The viscoelastic stress component τ_{11} is plotted along the height of the printed strand in Fig. 15b. The findings indicate that augmenting the heat transfer coefficient results in a corresponding elevation of stress. The heat flow into the bed primarily drives the cooling process at the bottom of the strand, which is consistently rapid due to its unaffected convective heat transfer coefficient. Increased convective heat transfer coefficients accelerate the dissipation of heat from the flowing molten polymer, resulting in a shorter period of stress relaxation. The figure, labeled as Fig. 15b, illustrates the relationship between the convective heat transfer coefficient and the magnitude of stresses. It demonstrates that higher convective heat transfer coefficients lead to higher stresses. An increased convection coefficient leads to higher stresses within the printed strand, negatively impacting print quality by promoting warping, reducing interlayer adhesion, and degrading surface finish. To mitigate these effects, it is crucial to optimize cooling conditions and balance the convection coefficient to match the material properties and part geometry. Controlled cooling strategies, such as localized cooling or heated build chambers, can help minimize the adverse effects.

4.6 Printing speed

Computational simulations were conducted to investigate the impact of printing velocity on stresses in the printed strand. The simulations were conducted with the specified parameters and a volumetric flow rate ($\dot{Q}$) of 20 mm^3/s, printing speeds of 40 mm/s and 60 mm/s. For stress extraction, the black vertical line in Fig. 10 is used. Figure 16a displays the plot of the viscoelastic stress tensor component τ_{11} along the height of the printed strand. As illustrated in Fig. 16a, the increase in printing speed leads to an elevation in stresses. The increase in printing speed leads to a higher stretching rate of the polymer chains in the polymer flow, causing an elevation in stresses. Increased printing speed leads to higher stress levels within the printed strand, negatively affecting print quality by reducing interlayer adhesion, increasing warping, and compromising dimensional accuracy and surface finish. These effects emphasize the need for careful optimization of printing speed, balancing throughput with the mechanical and aesthetic requirements of the final part.

4.7 Nozzle temperature

In order to examine the impact of nozzle temperature on stresses in the printed strand, simulations were conducted using the parameters described before, with nozzle

temperatures set at 473 K and 488 K. For stress extraction, the black vertical line in Fig. 10 is used. Figure 16b displays the plotted viscoelastic stress component τ_{11} along the height of the printed strand. As depicted in Fig. 16b, elevating the nozzle temperature resulted in a reduction of stresses. The decreased stresses can be attributed to the polymer flow holding a higher temperature for longer durations at elevated nozzle temperatures, which provides additional time for stress relaxation in the printed strand. Increasing the nozzle temperature and thereby reducing stress within the strand improves print quality by enhancing interlayer bonding, minimizing warping, and achieving better dimensional accuracy. However, the nozzle temperature must be optimized to avoid material degradation, over-extrusion, and dimensional inaccuracies, ensuring a balance between stress reduction and print integrity.

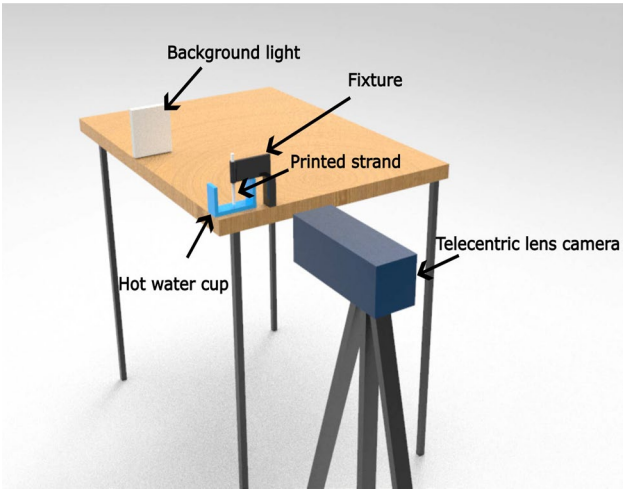

Fig. 17 Experimental set up for the qualitative validation of simulation results

5 Experimental method

The preceding section discussed how the printing process parameters affect the simulation of stresses in the printed strand. To qualitatively validate these findings, the experiments used a Prusa i3 MK3 printer and PLA filament. The strand samples were printed at different velocities (40 mm/s, 50 mm/s, and 60 mm/s) while maintaining consistent values for other parameters, including flow rate, nozzle temperature, and bed temperature, as in the simulation. Three samples were produced for each printing speed, each consisting of a single layer and a single strand, each 10 cms long. After printing, the samples were cooled down and removed from the print bed. Upon removal from the print bed, none of the samples showed any signs of deformation. After the printed strands were removed from the print bed, the ends of the printed strand were cut by 30 mm, and the 10 mm strand was fixed in the fixture as shown in the schematic diagram.

The experimental setup, depicted in Fig. 17, consisted of a telecentric lens camera, a fixture for securing the printed strand, a background illuminated with white light, and a container of hot water. The aforementioned components were employed to monitor the deformation that occurs when the temperature exceeds the glass transition temperature. This method allows for indirect measurement of stresses in the printed strand. The experimental setup involved securing a printed strand in fixture, leaving one end free, then submerging it in hot water to monitor its deformation. Daheng Imaging's MER2-502-79U3M (monochrome) camera was used to record the deformation process. This camera produces black-and-white output, as shown in Fig. 18. In Matlab, a camera recording of the deformation process is imported. The initial and final frames were saved as a PNG file for comparison once the complete deformation process was finished. The length of the fixed end was consistently maintained across all samples, and the outcomes for various printing speeds are depicted in Fig. 18. As can be observed in Fig. 18, the deformation of the printed strand when it was submerged in hot water demonstrates a distinct pattern of increasing distortion with increasing printing speeds. The observed increase in deformation can be attributed to an elevated level of stress. The aforementioned phenomenon has also been documented by Wu et al. [32] in their study. When immersing the printed strand in hot water, the researchers also observed a positive correlation between printing speed and distortion.

To indicate the degree of deformation in Fig. 19, the dotted line circle is added using the vector graphics editor Inkspace. All nine samples were imported into Inkscape and fitted with circles to measure radii. Table 3 displays the measured average radii for samples printed at 40 mm/s, 50 mm/s, and 60 mm/s. As the printing speed increases, the distorted strand's radius decreases. The experimental findings indicate that as the printing speed was raised from 40 to 60 mm/s, the radius of the distorted strand decreased by 41 %. According to the established relationship between beam curvature and bending moment, an increase in curvature results in an increase in bending moment. The bending moment and bending stress exhibit a direct proportionality. The stress distribution is used to figure out the bending moment, which can be seen in Fig. 16a and is shown in Table 3. Based on the computed bending moments for the strands printed at speeds of 40 mm/s and 60 mm/s, there is a roughly 104 % rise in the bending moment as the printing speed increases from 40 to 60 mm/s. As printing speed increases, the simulations overestimate the increase in the bending moment. The experimental and simulation results exhibit a consistent general pattern, with the simulations

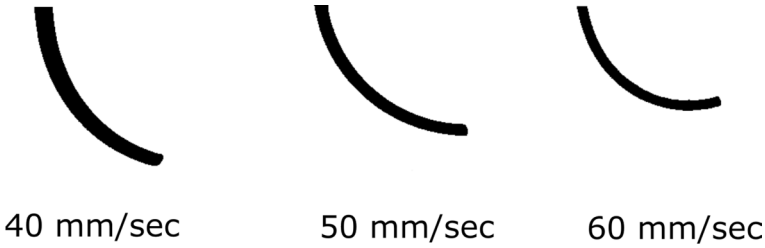

Fig. 18 Deformation of strands printed at different printing speed when they are subjected to temperature higher than the glass transition temperature of PLA

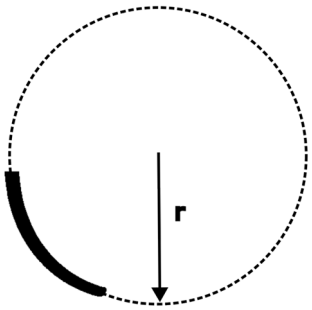

Fig. 19 The dashed circle is incorporated into the photo during post-processing to visually represent the curvature

Table 3 Quantification of the bending of deformed strands

Printing speed	40 mm/s	50 mm/s	60 mm/s
Avg. radius	27.33 mm	20 mm	16 mm
Bending moment (from simulations)	0.102 Nmm	0.152 Nmm	0.208 Nmm

providing an explanation for the observed one-layer memory effect in the experiment. At its current stage, the simulation methodology is not suitable for describing warping phenomena, as it is limited to single-layer strand simulations. Further development would be required to extend its applicability to multi-layered structures and comprehensive warping analysis.

6 Conclusions and outlook

The objective of this study was to improve the comprehension of material extrusion process modeling by examining the use of material models and stresses in the printed strand. A simulation model was created to study the material extrusion process. The influence of different constitutive models, such as the generalized Newtonian and viscoelastic models, on the stresses in the printed strand was examined. The polymer flow was simulated as a single-phase flow, with the different polymer phases differentiated primarily by their variable viscosity and relaxation time, which are dependent on the temperature and shear rate. During the polymer's passage through the liquefier, nozzle, and print bed, it undergoes stretching and relaxation, which generates stresses. These stresses remain in the printed strand as the polymer cools down. Using a viscoelastic material model, the simulation projected a non-uniform stress distribution over the printed strand's height. When exposed to a temperature higher than PLA's glass transition temperature, the uneven distribution of stress causes the printed strand to bend towards the print bed. Using numerical models, the study also investigated the influence of different printing process variables, such as bed temperature, nozzle temperature, printing speed, and convection coefficient, on stresses in the printed strand. Numerical analysis of the material extrusion process utilizing viscoelastic material models plays a critical role in accurately predicting stress evolution within printed strands. By effectively analyzing and controlling stress distributions, this approach facilitates the design and fabrication of components with highly predictable and functional stress-induced transformations. Such capabilities significantly enhance the performance and broaden the applicability of 4D-printed parts across diverse fields, including aerospace, robotics, biomedical engineering, and consumer products. Experimental validation was performed by utilizing PLA material and a Prusa i3 MK3 printer. Three strands were printed at varying printing speeds and subsequently submerged in hot water. The increased printing speed resulted in a reduction in the distorted printed filament's radius. This observation suggests that as printing speed increases, the stress in the printed strand also rises. The simulation findings demonstrate a positive correlation between printing speed and bending moment, indicating that an increase in printing speed leads to an increase in bending moment.

At its current stage, the simulation methodology is not suitable for describing warping phenomena, as it is limited to single-layer strand simulations. Further development would be required to extend its applicability to multi-layered structures and comprehensive warping analysis.

An investigation into the bridging in the material extrusion process is intended to be carried out as an extension of this work. The goal is to investigate the impact of various printing process factors on bridging through simulations and tests. As a continuation of this work, it intends to concentrate on printing a single strand in order to investigate the cooling behavior and adhesion using a variety

of nozzle sizes. Accurate thermal history prediction will enable to optimize layer time and printing speed for the large-scale fused granular fabrication additive manufacturing processes.

Acknowledgements This research is a part of FLAD-3D project which is supported by dtec.bw - Centre for Digitisation and Technology Research of University of Bundeswehr Munich. dtec.bw is funded by the European Union - NextGenerationEU. This work is also supported by the European Research Council through the H2020 ERC Consolidator Grant 2019 n. 864482 FDM^2.

Funding Open Access funding enabled and organized by Projekt DEAL.

Data availability Data sets generated during the current study are available from the corresponding author on reasonable request.

Declarations

Conflict of interest On behalf of all authors, the corresponding author states that there is no conflict of interest.

References

1. Gibson I, Rosen D, Stucker B (2015) Additive manufacturing technologies: 3D printing, rapid prototyping, and direct digital manufacturing, 2nd edn. Springer, New York. https://doi.org/10.1007/978-1-4939-2113-3
2. Bellini A (2002) Fused deposition of ceramics: a comprehensive experimental, analytical and computational study of material behavior, fabrication process and equipment design. Drexel University
3. Turner BN, Strong R, Gold SA (2014) A review of melt extrusion additive manufacturing processes: I. Process design and modeling. Rapid Prototyping J 20(3):192–204. https://doi.org/10.1108/RPJ-01-2013-0012
4. Ji LB, Zhou TR (2010) Finite element simulation of temperature field in fused deposition modeling. Adv Mater Res 97:2585–2588 (**Trans Tech Publ**)
5. AtifYardimci M, Hattori T, Guceri SI, Danforth SC (1997) Thermal analysis of fused deposition. In: 1997 International Solid Freeform Fabrication Symposium
6. Ramanath H, Chua C, Leong K, Shah K (2008) Melt flow behaviour of poly-ε-caprolactone in fused deposition modelling. J Mater Sci Mater Med 19(7):2541–2550
7. Mostafa N, Syed HM, Igor S, Andrew G (2009) A study of melt flow analysis of an abs-iron composite in fused deposition modelling process. Tsinghua Sci Technol 14:29–37
8. Osswald TA, Puentes J, Kattinger J (2018) Fused filament fabrication melting model. Addit Manuf 22:51–59
9. Doi M, Edwards SF (1988) The theory of polymer dynamics, vol 73. Oxford University Press
10. McLeish T, Larson R (1998) Molecular constitutive equations for a class of branched polymers: the pom-pom polymer. J Rheol 42(1):81–110
11. Inkson N, McLeish T, Harlen O, Groves D (1999) Predicting low density polyethylene melt rheology in elongational and shear flows with "pom-pom" constitutive equations. J Rheol 43(4):873–896
12. Wapperom P, Keunings R (2001) Numerical simulation of branched polymer melts in transient complex flow using pom-pom models. J Nonnewton Fluid Mech 97(2–3):267–281
13. Sirakov I, Ainser A, Haouche M, Guillet J (2005) Three-dimensional numerical simulation of viscoelastic contraction flows using the pom-pom differential constitutive model. J Nonnewton Fluid Mech 126(2–3):163–173
14. Verbeeten WM, Peters GW, Baaijens FP (2001) Differential constitutive equations for polymer melts: the extended pom-pom model. J Rheol 45(4):823–843
15. Tanner RI, Nasseri S (2003) Simple constitutive models for linear and branched polymers. J Nonnewton Fluid Mech 116(1):1–17
16. Pivokonsky R, Zatloukal M, Filip P, Tzoganakis C (2009) Rheological characterization and modeling of linear and branched metallocene polypropylenes prepared by reactive processing. J Nonnewton Fluid Mech 156(1–2):1–6
17. Ganvir V, Gautham B, Thaokar R, Lele A, Pol H (2011) Numerical and experimental studies on extrudate swell of branched polyethylene through axisymmetric and planar dies. Polym Eng Sci 51(11):217–221. https://doi.org/10.1515/polyeng.2011.046
18. Phan DD, Swain ZR, Mackay ME (2018) Rheological and heat transfer effects in fused filament fabrication. J Rheol 62(5):1097–1107
19. Serdeczny MP, Comminal R, Mollah MT, Pedersen DB, Spangenberg J (2022) Viscoelastic simulation and optimisation of the polymer flow through the hot-end during filament-based material extrusion additive manufacturing. Virtual Phys Prototyping 17(2):205–219
20. Serdeczny M (2020) Numerical and experimental analysis of filament-based material extrusion additive manufacturing. PhD thesis
21. Xia H, Lu J, Tryggvason G (2019) A numerical study of the effect of viscoelastic stresses in fused filament fabrication. Comput Methods Appl Mech Eng 346:242–259
22. Watanabe N (2016) Computational and experimental investigation of reinforced polymers for material extrusion additive manufacturing. PhD thesis, Georgia Institute of Technology
23. Comminal R, Serdeczny MP, Pedersen DB, Spangenberg J (2018) Numerical modeling of the strand deposition flow in extrusion-based additive manufacturing. Addit Manuf 20:68–76
24. Liu J, Anderson KL, Sridhar N (2020) Direct simulation of polymer fused deposition modeling (fdm)-an implementation of the multi-phase viscoelastic solver in openfoam. Int J Comput Methods 17(01):1844002
25. Xia H, Lu J, Tryggvason G (2018) Fully resolved numerical simulations of fused deposition modeling. Part ii–solidification, residual stresses and modeling of the nozzle. Rapid Prototyping J 24(2):463–476. https://doi.org/10.1108/RPJ-03-2017-0043
26. McIlroy C, Olmsted PD (2017) Deformation of an amorphous polymer during the fused-filament-fabrication method for additive manufacturing. J Rheol 61(2):379–397

27. Armillotta A, Bellotti M, Cavallaro M (2018) Warpage of fdm parts: experimental tests and analytic model. Robot Comput-Integr Manuf 50:140–152
28. Xinhua L, Shengpeng L, Zhou L, Xianhua Z, Xiaohu C, Zhongbin W (2015) An investigation on distortion of pla thin-plate part in the fdm process. Int J Adv Manuf Technol 79:1117–1126
29. Zhang Y, Chou K (2008) A parametric study of part distortions in fused deposition modelling using three-dimensional finite element analysis. Proc Inst Mech Engi Part B J Eng Manuf 222(8):959–968
30. Wang T-M, Xi J-T, Jin Y (2007) A model research for prototype warp deformation in the fdm process. Int J Adv Manuf Technol 33:1087–1096
31. Van Manen T, Janbaz S, Zadpoor AA (2017) Programming 2d/3d shape-shifting with hobbyist 3d printers. Mater Horiz 4(6):1064–1069
32. Wu P, Yu T, Chen M, Hui D (2022) Effect of printing speed and part geometry on the self-deformation behaviors of 4d printed shape memory pla using fdm. J Manuf Process 84:1507–1518
33. Barocio E, Brenken B, Favaloro A, Bogdanor M, Pipes RB (2020) Extrusion deposition additive manufacturing with fiber-reinforced thermoplastic polymers. In: Friedrich K, Walter R (eds) Structure and properties of additive manufactured polymer components. Elsevier, pp 191–219. https://doi.org/10.1016/B978-0-12-819535-2.00008-9
34. Bird RB, Armstrong RC, Hassager O (1987) Dynamics of polymeric liquids, vol 1. Fluid mechanics, 2nd edn. Wiley
35. Rudolph N, Osswald TA (2014) Polymer rheology: fundamentals and applications. Carl Hanser Verlag GmbH Co KG
36. Duty C, Ajinjeru C, Kishore V, Compton B, Hmeidat N, Chen X, Liu P, Hassen AA, Lindahl J, Kunc V (2018) What makes a material printable? a viscoelastic model for extrusion-based 3d printing of polymers. J Manuf Process 35:526–537
37. Thien NP, Tanner RI (1977) A new constitutive equation derived from network theory. J Nonnewton Fluid Mech 2(4):353–365
38. Djellali S, Sadoun T, Haddaoui N, Bergeret A (2015) Viscosity and viscoelasticity measurements of low density polyethylene/poly (lactic acid) blends. Polym Bull 72(5):1177–1195